P-ISSN: 2798-1134 | E-ISSN: 2797-3549 | DOI: 10.52562/injoes.2024.1043

Indonesian Journal of Earth Sciences

http://journal.moripublishing.com/index.php/injoes

| Research Article |

Petrographic and Diffractometric Analysis of Drill Samples from the Iron Ore Deposits of Zatua Hills, Haut Uélé Province, DRC

Levesque Makuku Mbo [1,2], Albert Ongendangenda Tienge [3]

[1]*Geological and Mining Researches Center (CRGM), Kinshasa, DR Congo*

[2]*Oil Exploration and Production Department, Faculty of Oil, Gas and Renewable Energies, University of Kinshasa, DR Congo*

[3]*Department of Geosciences, Faculty of Science and Technology, University of Kinshasa, B.P. 190 Kinshasa XI, DR Congo*

**Correspondence: levesquemakuku@gmail.com*

Received: 15 May 2024 / Accepted: 02 August 2024 / Published: 09 September 2024

Abstract: Seven samples were selected from various facies of geological formations intersected by the drill holes for petrographic analysis, supplemented by diffractometry. The goal was to identify the mineralogical composition of Banded Iron Formations (BIFs), the associated parageneses, and elements deleterious to the metallurgical processing of iron ore. Field tests, based on geophysical maps, were conducted to identify high-prospectivity sites characterized by low magnetic susceptibility and hematite richness, followed by sampling and drilling to confirm mineralization. Selected samples from characteristic facies in contact with iron ores underwent petrographic analysis using optical and scanning electron microscopy, supported by diffractometric analyses to ensure accurate mineralogical identification. The study revealed the presence of hematitic BIF, predominantly composed of weakly aggregated euhedral and subhedral martite grains, with evidence of some leaching. Magnetite, identified as the protore mineral, has been oxidized by fluid influence into martite (hematite), with a low presence of secondary supergene minerals. Variscite, kaolinite, and gibbsite were the main secondary minerals identified in both petrographic and diffractometric analyses, and are considered sources of phosphorus, aluminum, and silica—elements recognized as harmful in the metallurgical processing of iron and its alloys. These secondary minerals were precipitated within interstitial cavities leached between martite and hematite aggregates, forming a botryoidal texture. The BIFs of the Zatua Hills are primarily composed of hematitic iron ores associated with goethite, microplaty hematite, and secondary supergene minerals, likely formed through fluid circulation along fracture zones, shearing, and folding. Geochemical studies are recommended to complete the analysis, aiming to determine the content of these iron oxides, secondary minerals, and the degree of hydration through loss on ignition.

Keywords: Iron ore, Petrography, Diffractometry, Zatua Hills, DRC

INTRODUCTION

The iron ores of Zatua Hills are primarily associated with Banded Iron Formations (BIFs) within the greenstone belt located in the northeastern part of the Democratic Republic of Congo (DRC). These BIFs are hosted in the Upper Congo Granites Complex, which includes two major geological units: the Lower Kibalian, comprising high-grade metamorphic series, basaltic volcanic rocks, and tonalite intrusions (>2.8 Ga) with a scarcity of BIFs and metasediments (Lavreau, 1984), and the Upper Kibalian, dominated by metasediments, extensive BIFs, rare volcanic rocks, and intruded granitic rocks (>2.45 Ga) (Lavreau & Ledent, 1975; Lavreau, 1980).

Zatua Hills are situated between 27°31'48" and 27°40'48" east longitude and 1°55'48" and 2°01'48" north latitude, within Wamba Territory, Haut-Uélé Province, DRC. The area is approximately 300 km from the city of Kisangani (Figure 1). Zatua Hills form part of a relatively small plateau with elevations ranging from 500 to 1,089 meters. The landscape features intermittent hills rising up to 300 meters above the surrounding plateau and a series of hills running NW-SE, including the Zatua Hills, with a maximum altitude of 1,300 meters. To the southeast, the area is bordered by the Western Rift Valley, encompassing Lakes Albert and Edward, separated by the Ruwenzori massif (5,119 meters).

The northeastern DRC is predominantly covered by Archean formations, which span approximately 500,000 km² and extend from the northern DRC into eastern Africa, including Uganda, southern Kenya, and northern Tanzania (Cahen & Snelling, 1966; Link et al., 2010; de Wit & Linol, 2015). These formations are remnants of a single geological block before the Ruwenzori chain (2 Ga) caused

their separation, followed by the filling of rift basins (Borg & Shackleton, 1997; Lavreau, 1982).

The Archean formations consist of 80-90% plutonic rocks and 10-20% volcano-sedimentary rocks, predominantly metamorphosed under greenschist facies conditions. These rocks form belts and isolated blocks that host major gold deposits, as documented in studies from the DRC (Woodtli, 1961; Cahen & Snelling, 1966; Lavreau, 1973, 1984; Cahen et al., 1984; Allibone et al., 2020), Tanzania (Manya et al., 2006; Chamberlain, 2003; Kabete et al., 2012a, b; Sanislav et al., 2014, 2015, 2017), and Uganda (Nyakecho & Hagemann, 2014; Westerhoff et al., 2014).

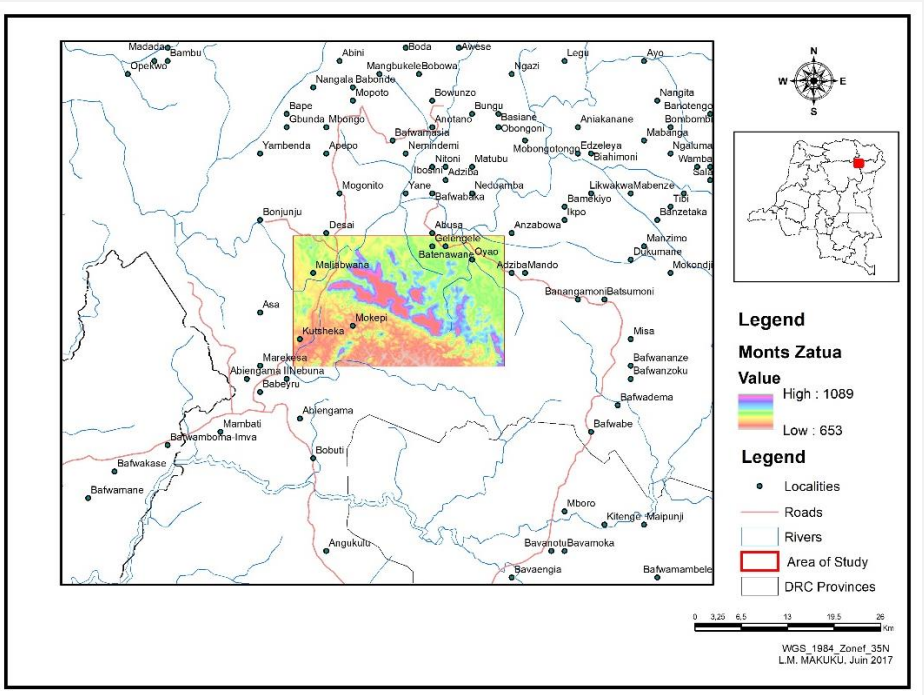

Figure 1. Location of Zatua Hills (Makuku et al., 2023).

Key geological formations in the region include the Garamba Complex, the Bomu amphibolitic and gneissic complex (3.4-3.7 Ga) (Cahen et al., 1984), the West Nile amphibolitic complex (3.2-2.7 Ga) (Allibone, 2020), and the Upper Congo Granites Massifs, which are composed of magmatic rocks, orthogneisses, and various magmatic intrusions. The Kibalian greenstone belt, part of these formations, hosts the BIFs of Zatua Hills, forming the core of the Archean units in the region (Lavreau, 1982; Cahen & Snelling, 1966; BRGM, 1982; Cahen et al., 1984; Bird, 2016; Allibone, 2020).

BIFs are the most prominent geological formations in the region, occupying extensive areas compared to other formations. Their presence is clearly depicted on the map in Figure 2. In some areas, these BIFs can reach up to 200 meters in thickness and are often associated with structural features such as folds, faults, and laminations, forming significant topographic relief. In certain locations, the BIFs are intercalated with schistose rocks above and basalts below (Makuku, 2018).

Published radiometric dating for rocks in northeastern DRC is limited, with eight Rb-Sr ages, many with uncertainties of 100-200 Ma or more (Cahen et al., 1984; Poidevin, 1985), and two U-Pb zircon ages (Manttari et al., 2013; de Wit & Linol, 2015) from the Archean-Neoproterozoic composite West Nile gneiss, northeast of the Moto and Kibali belts.

Research by Randgold has identified three suites of Neoarchean granitoids with distinct chemical compositions in northeastern DRC: (1) Ca- and Na-rich tonalites, trondhjemites, and granodiorites with high Sr/Y ratios; (2) less sodic, more potassic granodiorites and granites with low Sr/Y ratios; and (3) Fe-, Zr-, Y-, and Nb-rich monzodiorites, tonalites, granodiorites, and quartz granites with both low and high Sr/Y ratios (Turnbull et al., 2017; Allibone et al., 2020). The first two suites are comparable to the high- and low-Ca granitoids of many Neoarchean terrains (Champion & Sheraton, 1997), while the third suite resembles those found in the eastern Yilgarn craton, Western Australia (Czarnota et al., 2010).

These formations are overlain by Upper Proterozoic (Lindian), Mesozoic, and West African Rift formations of Cenozoic age.

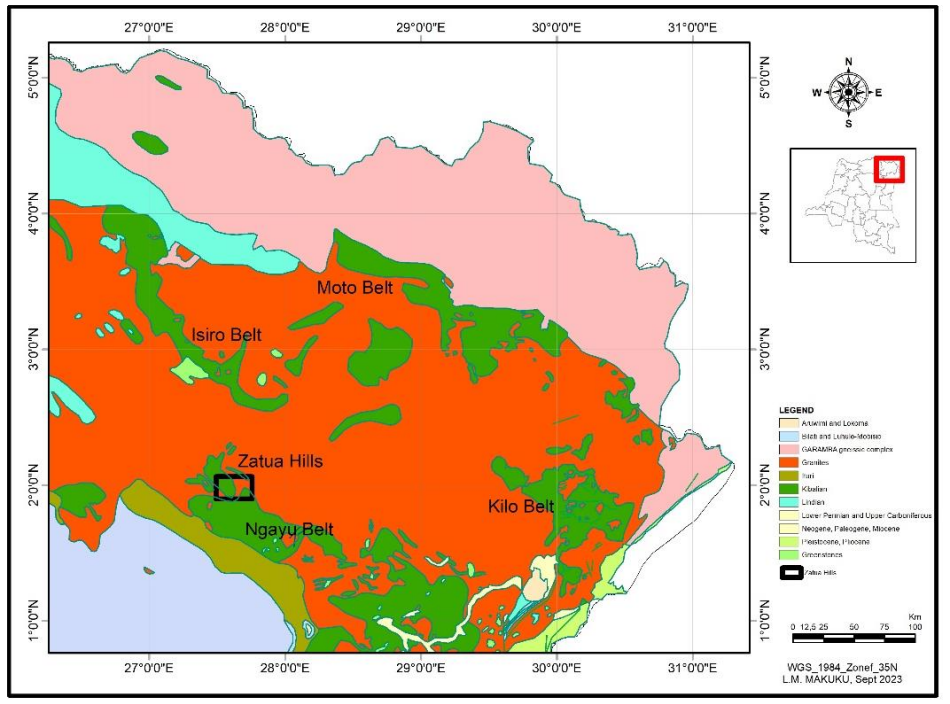

Figure 2. Regional Geological Map of Haut-Uelé Province (Makuku et al., 2023).

Identifying BIFs at depth remains a major challenge, limiting the ability to compare the mineralogical and petrographic characteristics of these rocks below the surface. Previous research in northeastern DRC has primarily focused on gold exploration, with geological studies providing limited information on iron ore deposits. These studies were confined to deposits surrounding gold mines, such as Moto, Kilo, Tina, and Zani, located north of our study area. Logistical constraints and the scarcity of visible gold deposits in the southern part of the greenstone belt have led to superficial studies of this region. The only recognized studies in this area involve reconnaissance of surface rocks, geochronology, and mapping (Woodtli, 1961; Lavreau, 1973; BRGM, 1982; Bird, 2016; Beukes et al., 2003; Allibone et al., 2020; Makuku et al., 2023).

This study aims to address this gap by contributing to the petrographic understanding of BIFs at depth, focusing on the mineral associations that often hinder the metallurgical processing of iron ores. The main objective is to elucidate the petrographic characteristics of BIFs in the Zatua Hills at depth, complementing existing research on surface rocks. This contribution will not only assist researchers in exploring other aspects of the genesis and depositional environments of these rocks but also aid the industry in assessing the quality of iron ore for extraction.

Specific Objectives are: (1) Conduct macroscopic observations of borehole samples to identify various minerals visible to the naked eye or under a magnifying glass; (2) Perform microscopic analyses using optical and scanning electron microscopes to identify the main mineral phases and those developed in circulation zones, which are considered both leaching and deposition zones for secondary minerals;(3) Support petrographic analysis results with diffractometry to determine the mineralogical composition of selected samples.

METHOD

Selection of the Study Area and Sampling Strategy

The study area was selected following a thorough review of previous work in the region, including geological and geophysical mapping of the BIFs. The focus was on outcrop areas and regions with low magnetic susceptibility in the Zatua Mountains. To ensure comprehensive petrographic analysis, six samples were selected based on the geological context, rock consistency, and the nature of the iron ore encountered in the drill holes. This selection was aimed at identifying the petrographic and mineralogical characteristics of the BIFs.

Analysis Techniques

The prepared samples were initially examined using a binocular microscope. Specific areas of interest were selected for the preparation of polished and thin sections, which were then analyzed using light microscopy and scanning electron microscopy (SEM).

- *Light Microscopy:* Each polished and thin section was systematically examined using conventional reflected and transmitted light microscopy. Individual minerals were identified based on their optical properties.
- *Scanning Electron Microscopy (SEM):* At least one polished section from each sample was systematically examined using SEM. Minerals were identified based on their chemical composition, determined through qualitative energy dispersive microbeam analyses.
- *X-ray Diffraction (XRD):* XRD analyses were conducted to determine the mineralogical composition of the samples. Prepared samples were analyzed using a Panalytical PW1840 diffractometer, operating with Fe-filtered Co Kα radiation. Instrumental settings were optimized to ensure accurate reflection resolution. Individual minerals were identified by comparing their diffraction patterns with a standard database.

Justification of Analytical Choices

- *Optical Microscopy:* This method allowed for the differentiation of various oxides and hydroxides present in the BIFs, as well as the identification of textures indicative of oxidation processes.
- *Scanning Electron Microscopy (SEM*): SEM provided high-resolution observations, enabling the identification of secondary mineral deposition phases in pores and stress zones, such as fractures, folds, and shear zones.
- *X-ray Diffraction (XRD):* XRD analyses were essential for determining the mineralogical composition of the BIFs, thereby supporting the petrographic analyses conducted on the same samples.

RESULTS

The samples collected in the field were subjected to diffractometric and petrographic analyses using optical and scanning electron microscopes. The findings are detailed below:

Petrographic Analysis

Sample SMZ 216

a. Macroscopic Sample Description

Sample SMZ 216 is a fragmented, hematite-rich Banded Iron Formation (BIF) that has undergone partial weathering (Figure 3). A white, clay-like phase is locally abundant and clearly visible in hand specimens. Despite extensive brecciation, some primary layering remains evident.

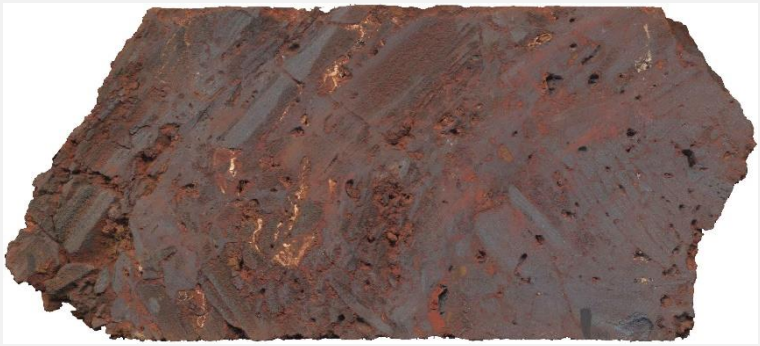

Figure 3. A color photograph illustrating the general nature and appearance of Sample SMZ 216 in hand specimen. Note the presence of minor amounts of a white, clay-like phase and the fragmented nature of the hematite-rich laminations. The width of view is approximately 14 cm.

b. Microscopic Sample Description

Detailed examination of this sample using a combination of optical microscopy and Scanning Electron Microscopy (SEM) confirmed that it predominantly consists of hematite, along with significant amounts of gibbsite and goethite (Figures 4a & 4b).

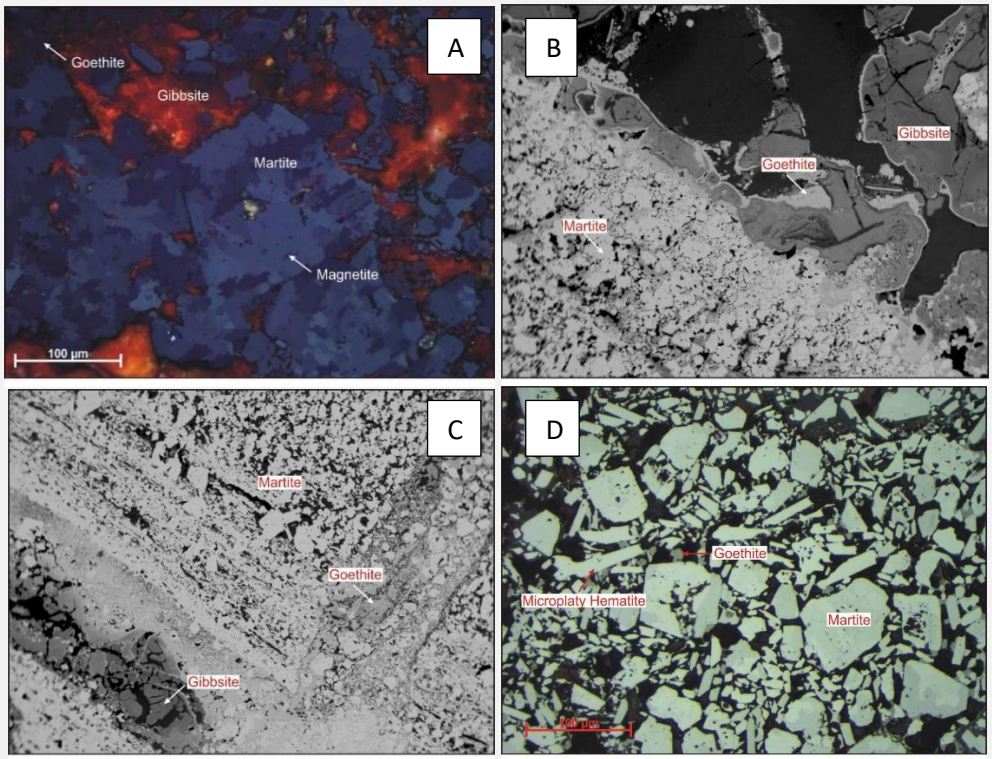

Figure 4. A) The same area illustrated in Figure 3 but under partially crossed polars, showing the discrete crystallites within the hematite/martite. The irregular grain boundaries of the martite crystallites indicate that equilibrium conditions were not attained. The width of view is approximately 400 µm. B) A backscattered electron image illustrating botryoidal and concretionary goethite (mid-grey) and gibbsite (dark grey) infilling a cavity in the porous hematite/martite aggregates (light grey). Pore spaces are black. The width of view is approximately 3 mm. C) A backscattered electron image showing discordant and concordant goethite- (mid-grey) and gibbsite- (dark grey) filled fractures and cavities associated with the porous martite-rich laminations (light grey). Pore spaces are black. The width of view is approximately 3 mm. D) A reflected light photomicrograph illustrating subhedral martite (light grey) and microplaty hematite laths with minor amounts of goethite (mid-grey shades). Pore spaces and gibbsite appear as undifferentiated dark grey/black. The width of view is approximately 400 µm.

The martite aggregates are traversed by numerous fractures, which are largely filled with martite, goethite, or gibbsite (Figure 4c). The martite grains show partial recrystallization, with trellis textures being rare (Figure 4a). The hematite/martite crystallites exhibit irregular grain boundaries, indicating that equilibrium conditions were not reached during recrystallization (Figure 4a). These martite aggregates also display a high degree of porosity (Figures 4a & 4c). Martite grains commonly exhibit partial to extensive oxidation and replacement by goethite, particularly in the more porous regions of the sample (Figure 4b). Microplaty/specular hematite is present in relatively minor amounts, occurring in the interstitial regions between martite grains (Figure 4d). Minor amounts of relict magnetite are disseminated throughout the martite (Figures 4a & 4c).

Martite is a term used to describe hematite pseudomorphs after identifiable magnetite (Gruner, 1926; Davis et al., 1968), without implying the specific genetic timing or process. The context of its use has been discussed by Tompkins & Cowan (2001) and Morris et al. (2002). In this sample, martite grains show partial recrystallization and a high degree of porosity.

Microplaty hematite typically consists of crystalline platelets measuring 10 to 200 µm, forming a three-dimensional network with intragranular porosity (Clout & Simonson, 2005). It is present in minor amounts within this sample.

Gibbsite is a common accessory phase, predominantly occurring as a cavity infill (Figures 4b & 4c). In this sample, gibbsite is locally abundant, filling larger cavities between the porous martite aggregates. It is easily observed in hand specimens, where it exhibits a distinctive pinkish-white color (Figure 3). Qualitative SEM analysis indicates that gibbsite often shows varying degrees of ferruginization, which likely represents partial replacement or fine intergrowths with goethite. Additionally, minor amounts of silicon were detected in the gibbsite.

Goethite, commonly found in this sample, exhibits a distinctive orange-brown color in hand specimens (Figure 3). It occurs as a partial replacement of martite and forms botryoidal and concretionary aggregates within the larger cavities and pore spaces between the martite aggregates (Figure 4). Botryoidal textures are typical of open-space deposition. Qualitative SEM analysis of goethite revealed minor amounts of aluminum, phosphorus, and titanium. Both gibbsite and goethite represent relatively late stages of mineralization, likely precipitated from oxidizing fluids under near-surface weathering conditions.

Sample SMZ 217

a. Macroscopic Sample Description

Sample SMZ 217 consists of a delicately layered hematitic Banded Iron Formation (BIF) interspersed with massive quartz-rich layers (Figure 5). The quartz/chert appears to partially replace the hematite-rich layers.

Figure 5. A color photograph illustrating the general nature and appearance of this sample in hand specimen. The quartz/chalcedony layers (pinkish white) appear to replace the hematite-rich layers (dark reddish grey) along discordant fractures close to the contact zone. The width of view is approximately 13 cm.

b. Microscopic Sample Description

Transmitted light microscopy of the quartz/chert reveals that it is cryptocrystalline (chalcedony) (Figure 6a) and exhibits localized recrystallization, leading to an increase in crystallite size. Recrystallized chalcedony/quartz veinlets cut through the more massive, fine-grained chalcedony and also replace hematite-rich laminations along discordant fractures and concordant separations in the hematitic BIF (Figure 6c). The quartz/chert appears to represent a later stage of mineralization than the hematitic BIF and may have formed through the dissolution and subsequent re-precipitation of primary silicate gangue minerals.

The hematitic BIF consists primarily of massive aggregates of martite, forming discrete layers ranging in width from a few micrometers to several millimeters (Figure 6c). The martite has undergone some degree of recrystallization, with partially recrystallized lattice textures observed in localized areas (Figure 6d).

The martite layers are often intersected by numerous discordant fractures, some of which are partially filled with chalcedony (Figure 6c). Automorphic martite crystals are present locally, particularly in the chalcedony-rich parts of the sample, and likely represent former magnetite grains disseminated in the gangue-rich sections of the primary BIF (Figure 6b). Specular/microplaty hematite crystals are present in small quantities, typically within fractures in martite-rich layers, and are associated with chalcedony/quartz (Figure 6c). Additionally, fine-grained relict magnetite is sparsely distributed within the martite layers (Figure 6b).

A SiAl-containing clay, likely from the kaolinite group, is commonly associated with chalcedony (Figures 6a & 6b). Chalcedony also contains subordinate but significant amounts of a CeAl-phosphate mineral, probably florencite ((Ce, La) $Al_3(PO_4)_2(OH)_6$), a member of the crandallite group, which often forms as a result of the weathering and replacement of apatite (Figures 6a & 6b).

Sample SMZ 218

a. Macroscopic Sample Description

Sample SMZ 218 consists of a porous and friable itabirite, rich in hematite, with a delicate layering that primarily reflects variations in porosity (Figure 7). Minor amounts of a white clay phase are present locally.

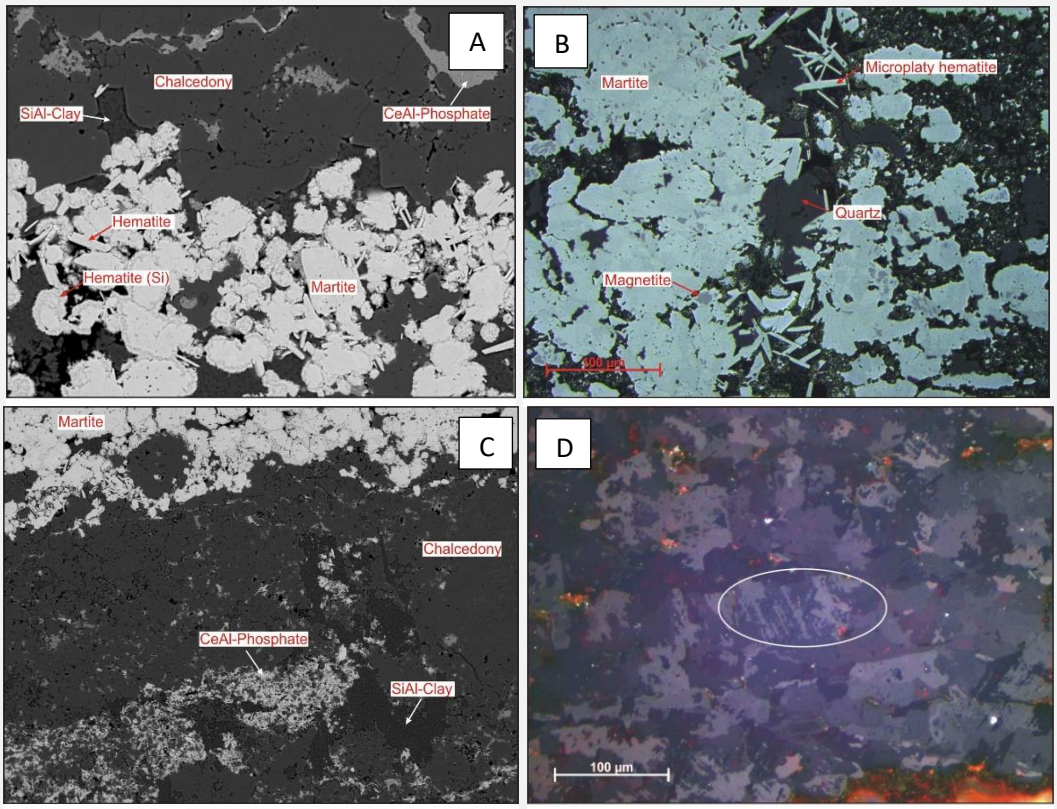

Figure 6. A) A backscattered electron image illustrating CeAl-phosphate (mid grey) in chalcedony (mid/dark grey). Si-bearing hematite (mottled light grey) forms spheroids and rims on the martite (light grey). Microplaty hematite and SiAl-clay (darkest grey) are also present. The width of view is approximately 250 μm. B) A reflected light photomicrograph illustrating microplaty/specular hematite laths partially filling a small fracture in a recrystallized martite layer (light grey). Quartz/chalcedony (dark grey) is also present in the fracture. Relict magnetite (mid grey) is associated with the martite. The width of view is approximately 400 μm. C) A backscattered electron image illustrating the presence of CeAl-phosphate (probably florencite, mid/light grey) and SiAl-clay (dark grey) in a chalcedony/quartz- (mid/dark grey) rich portion of the sample. The width of view is approximately 800 μm. D) A reflected light photomicrograph under partially crossed polars illustrating partially recrystallized trellis textures in the hematite/martite (circled). The width of view is approximately 400 μm.

Figure 7. A color photograph illustrating the general nature and appearance of this sample in hand specimen. Note the sugary texture exhibited by the core, largely due to the porous and granular nature of the martite. The width of view is approximately 10 cm.

b. Microscopic Sample Description

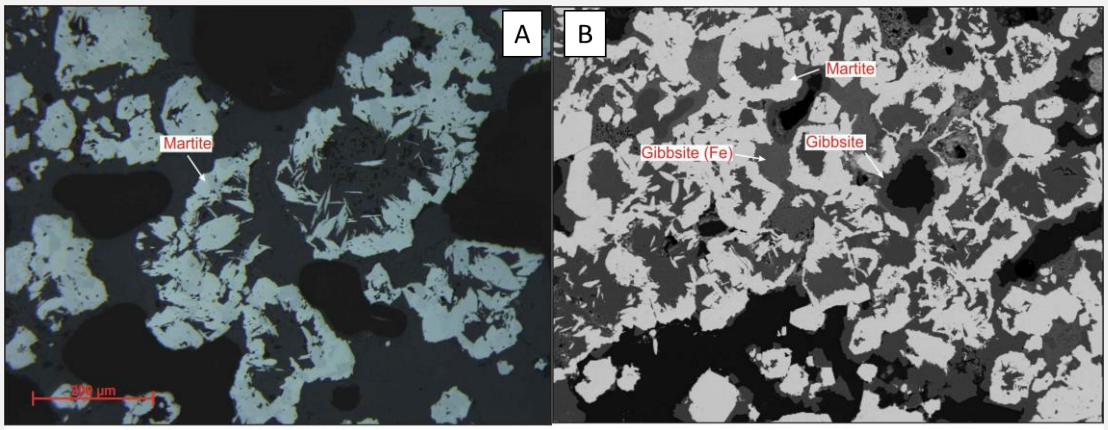

Figure 8. A) A reflected light photomicrograph illustrating recrystallized skeletal martite grains (light grey). The martite has been partially replaced by small bladed crystals of hematite. The interstitial regions consist of gibbsite, pore spaces, and epoxy resin (poorly differentiated dark grey/black). The width of view is approximately 800 μm. B) A backscattered electron image illustrating weakly aggregated skeletal martite grains (light grey) and interstitial gibbsite (dark grey shades). The lighter grey shades in the gibbsite reflect elevated levels of Fe. Pore spaces are black. The width of view is approximately 1 mm.

The mineralogy of this sample is relatively simple, consisting predominantly of weakly aggregated euhedral and subhedral martite grains, along with subordinate amounts of interstitial gibbsite (Figure 8b). Locally, the martite appears to have undergone some degree of leaching, resulting in skeletal textures (Figure 8a). The martite grains vary widely in size, though they rarely exceed 350 μm.

The delicate layering observed in the hand sample is largely due to variations in the porosity and grain size of the martite. Relict lattice textures are essentially absent, with the martite displaying recrystallization textures (Figures 8a & 8b). The martite crystallites exhibit irregular grain boundaries, indicating that recrystallization did not reach equilibrium conditions. Detailed examination of the skeletal martite grains confirms that recrystallization resulted in the development of micro-platelets (Figure 8a). These micro-flattened textures appear to be the result of recrystallization rather than enrichment by supergene fluids. Traces of magnetite are present within the martite.

Gibbsite is the dominant phase in the interstitial regions between the martite grains (Figure 8b). The gibbsite likely formed due to near-surface alteration and subsequent precipitation from Al-rich fluids at low temperatures. Qualitative SEM analysis of the gibbsite confirms that it typically contains minor but variable amounts of Fe (Figure 8b).

Sample SMZ 219

a. Macroscopic Sample Description

Sample SMZ 219 consists of a hematite-rich, robust itabirite with prominent layering that largely reflects variations in porosity and grain size (Figure 9). A mottled texture was also noted during field observations.

Figure 9. A color photograph illustrating the general nature and appearance of this sample in hand specimen. The delicate layering appears to reflect, in part, significant variations in porosity. The less porous hematite may also cross-cut the more porous laminations. The width of view is approximately 11 cm.

b. Microscopic Sample Description

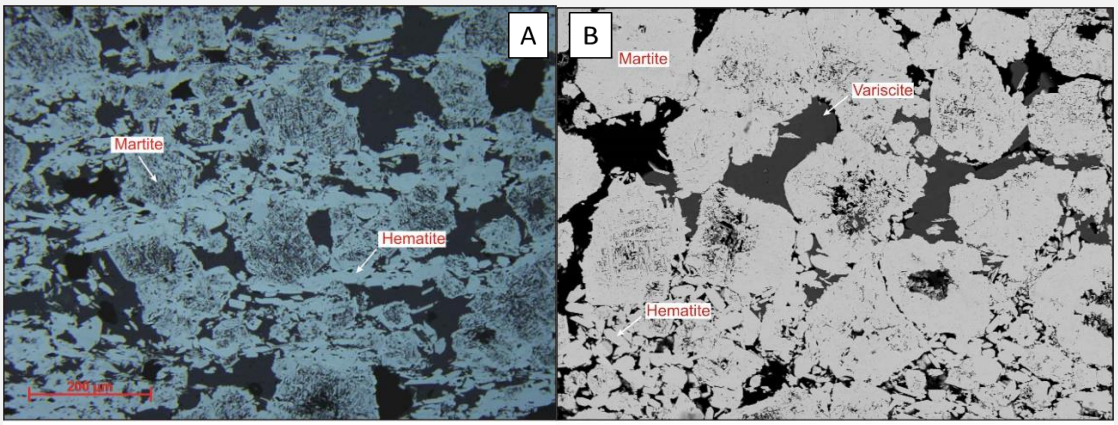

Figure 10. A) A reflected light photomicrograph illustrating porous martite grains together with interstitial hematite (light grey). Note the characteristic trellis texture exhibited by the martite. The hematite platelets exhibit a preferred orientation. The width of view is approximately 800 µm. B) A backscattered electron image illustrating minor amounts of variscite ($AlPO_4 \cdot 2H_2O$) partially filling pores (black) between martite grains (light grey). Microplaty hematite is also present in the field of view. The width of view is approximately 500 µm.

This sample is dominated by the presence of martite and hematite. The more porous laminations consist of extensively leached martite grains along with subordinate amounts of microplaty/fine tabular hematite grains (Figure 10b). In contrast, the less porous laminations are predominantly composed of microplaty/fine tabular hematite grains with subordinate amounts of martite (Figures 10a & 10b).

The microplaty/fine tabular hematite grains appear to represent a later stage of hematite enrichment and often cross-cut the more porous martite-rich layers (Figure 10). These hematite grains rarely exceed 100 µm in length and generally exhibit a random orientation. However, a weak preferred orientation is observed in the tabular hematite within the porous martite-rich layers (Figure 10a).

Although the bulk of the martite occurs as extremely porous/leached grains, a subordinate portion is present as more robust euhedral and subhedral grains (Figure 10b). Trellis textures, which are characteristic of martite, have been effectively obliterated in the more robust martite grains due to recrystallization. However, these textures remain clearly evident in the porous/leached martite (Figure 10).

Relict magnetite was not observed in the microscopic examination. Minor amounts of variscite ($AlPO_4 \cdot 2H_2O$) were detected, partially filling cavities within the martite-rich porous layers (Figure 10b).

Sample SMZ 220

a. Macroscopic Sample Description

Sample SMZ 220 consists of a hematitic itabirite (BIF) with delicate and poorly defined stratification. The BIF is in direct contact with a largely ferruginized reddish-brown lithology (Figure 11). The contact between the two lithologies is marked by a white clay layer about 1 mm wide, which is also present along narrow fractures in the hematitic BIF.

Figure 11. A color photograph illustrating the general nature and appearance of this sample in hand specimen. The width of view is approximately 17 cm.

b. Microscopic Sample Description

Detailed examination of the BIF component of this sample confirms that it consists of disseminated euhedral and subhedral martite grains cemented by subordinate amounts of microplaty hematite (Figures 12a & 12b). The BIF shows delicate layering, reflecting subtle variations in porosity, grain size, and the relative proportions of martite and microplaty hematite. The granular martite layers within the BIF exhibit a relatively high degree of porosity, with the interstitial regions between the martite grains largely filled by variscite (Figures 12b & 13b).

The variscite also shows weak compositional zonation, reflecting variations in the presence of minor amounts of Fe (Figure 12b). Most of the martite has undergone recrystallization, partially or largely replacing the lattice textures typical of the magnetite-to-hematite transformation. Minor amounts of relict magnetite are dispersed within the martite (Figure 12a).

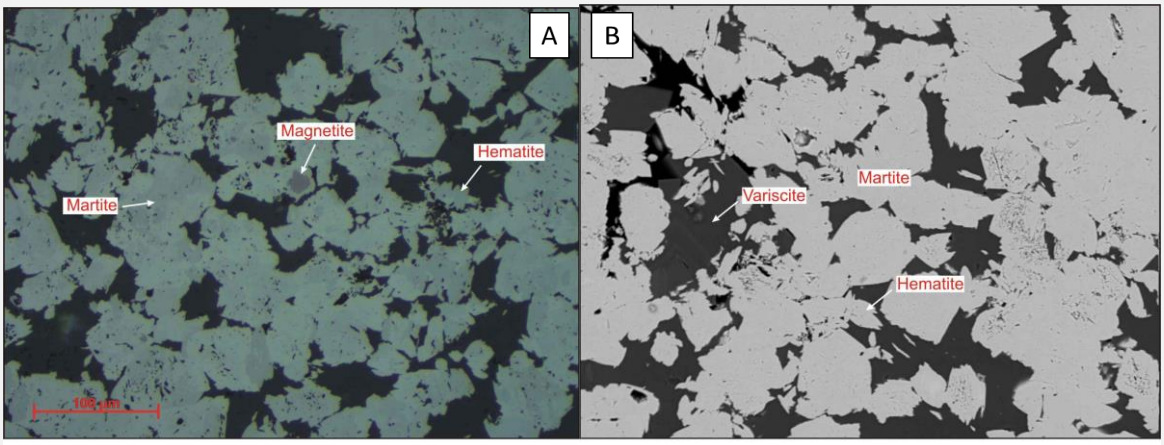

Figure 12. A) A reflected light photomicrograph illustrating the typical nature of the martite-rich BIF component of this sample, consisting of porous granular martite aggregates (light grey) cemented by minor amounts of hematite and interstitial variscite (dark grey, undifferentiated from cavities and epoxy resin). Minor amounts of relict magnetite (mid-pinkish grey) are also present. The width of view is approximately 400 μm. B) A backscattered electron image illustrating weakly zoned variscite (mid-grey shades) largely filling the cavities (black) between martite grains (light grey). Microplaty hematite cements the martite grains. The width of view is approximately 250 μm.

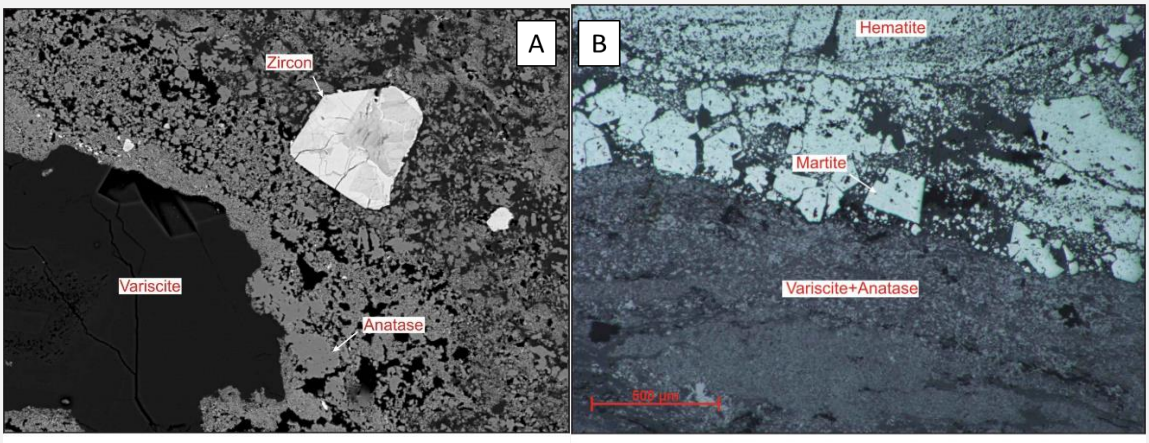

Figure 13. A) A backscattered electron image illustrating altered zircon grains (light grey) in the variscite (dark grey) and anatase (mid-grey) layer. Anatase-free variscite also appears to fill a cavity in this portion of the sample. The width of view is approximately 250 μm. B) A reflected light photomicrograph illustrating the contact between the BIF and white vein/reddish-brown lithology seen in Figure 11. The uppermost portion of the image consists of microplaty hematite layers. A coarse martite (light grey)/variscite (dark grey) layer (mid-portion of the image) exhibits a sharp contact with the white vein/reddish-brown lithology (undifferentiated lower portion of the image), which consists of variscite and anatase. The width of view is approximately 2 mm.

The less porous laminations of the BIF are dominated by fine-grained microplaty hematite crystals. These less porous laminations, compared to the martite-rich BIF, consist of randomly oriented microplaty hematite crystals that rarely exceed 40 μm in length (Figures 12a & 12b). Interstitial regions and cavities associated with finely crystalline hematite are typically partially filled by variscite (Figures 12b & 13a).

The BIF shows a relatively clear contact with the white clay vein (Figures 11 & 13b). The white clay vein consists mainly of variscite ($AlPO_4 \cdot 2H_2O$) and abundant fine anatase (TiO_2) outcrops (Figures 13a & 13b).

A number of accessory phases were observed in the reddish-brown lithology, including zircon ($ZrSiO_4$), baddelyite (ZrO_2), and a Ba and Sr sulfate that likely represents an intermediate member of the barite ($BaSO_4$) and celestite ($SrSO_4$) solid solutions (Figure 13a).

The variscite and anatase likely formed as a result of precipitation from low-temperature supergene fluids under near-surface weathering conditions. Variscite typically forms when P-bearing groundwaters react with Al-rich rocks in near-surface weathering conditions. Anatase, a low-temperature form of TiO_2, likely formed under the same conditions as variscite. Ti-bearing fluids generated during the oxidation and weathering of Ti-bearing oxides and silicates may precipitate anatase as Eh and pH conditions change lower in the weathering profile.

Sample SMZ 222

a. Macroscopic Sample Description

Sample SMZ 222 consists of a porous hematitic BIF in which the laminations are somewhat disaggregated and discontinuous (Figure 14). The BIF exhibits a wide variation in porosity at the local level. The textures observed in the hand sample largely reflect variations in porosity and grain size.

Figure 14. A color photograph illustrating the general nature and appearance of this sample in hand specimen. This laminated sample exhibits a somewhat fragmented appearance with a wide variation in porosity. The width of view is approximately 9 cm.

b. Microscopic Sample Description

The bulk mineralogy of this sample is simple, consisting of massive aggregates of recrystallized martite exhibiting varying degrees of fracturing, with microplaty hematite present in fractures and cavities (Figure 15). The discrete layers observed in the hand sample consist of massive recrystallized martite layers with relatively low porosity, rarely exceeding a few millimeters in width (Figure 14).

Traces of magnetite are disseminated in the martite. The recrystallized martite shows varying degrees of fracturing, likely resulting from localized collapse following the leaching of primary silicate minerals (Figures 15a & 15b).

Microplaty hematite typically forms an overgrowth on recrystallized martite aggregates, cementing the martite fragments together and locally reducing the porosity of the sample (Figures 15a & 15b). The microplaty hematite has a random orientation, and discrete crystals rarely exceed 75 μm in length.

Sample SMZ 227

a. Macroscopic Sample Description

Sample SMZ 227 consists of a soft, friable, fine-grained reddish-brown rock that exhibits

extensive ferruginization (Figure 16). A pinkish-white clay-like phase is abundant, occurring predominantly along narrow fractures.

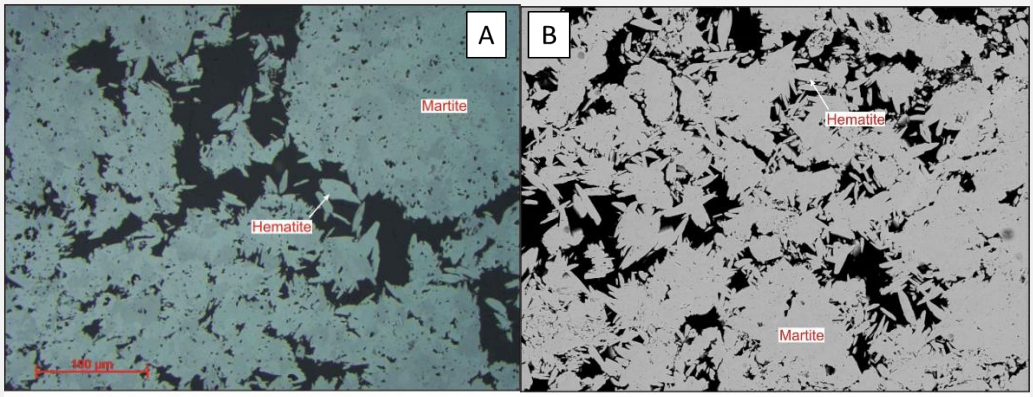

Figure 15. A) A reflected light photomicrograph illustrating microplaty hematite crystals forming overgrowths on the martite and partially filling fractures and cavities. The width of view is approximately 400 µm. B) A backscattered electron image illustrating microplaty hematite crystals forming overgrowths on the martite and partially filling fractures and cavities. The width of view is approximately 400 µm.

Figure 16. A color photograph illustrating the general nature and appearance of this sample in hand specimen. The width of view is approximately 7 cm.

b. Microscopic Sample Description

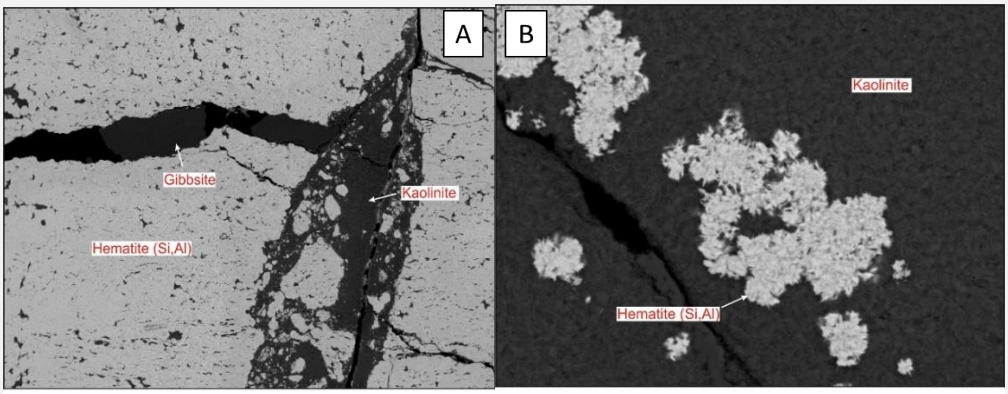

Figure 17. A) A backscattered electron image illustrating fine-grained Si- and Al-bearing hematite together with kaolinite (dark grey) and gibbsite (also dark grey) along prominent fractures. The width of view is approximately 1 mm. B) A backscattered electron image illustrating the fine-grained nature of spheroidal Si- and Al-bearing hematite aggregates that appear to have formed as a result of the extensive replacement of kaolinite (dark grey). The width of view is approximately 100 µm.

This sample consists predominantly of fine-grained Si- and Al-bearing hematite that appears to have formed as a result of the replacement of kaolinite (Figures 17a & 17b). Detailed examination confirms that the hematite is composed of fine-grained and porous spheroidal aggregates of plate-like crystals (Figure 17b). The presence of Si and Al likely reflects the inclusion of fine kaolinite within the hematite aggregates. Kaolinite and gibbsite are also abundant within the numerous fractures that traverse this sample (Figure 17a). This sample differs markedly from the previous samples in this suite and may represent a ferruginized weathered phyllite.

Diffractometric Analysis

Sample SMZ 216

X-Ray Diffraction (XRD) analysis confirms that this sample consists predominantly of hematite, gibbsite, and subordinate amounts of goethite (Figure 18).

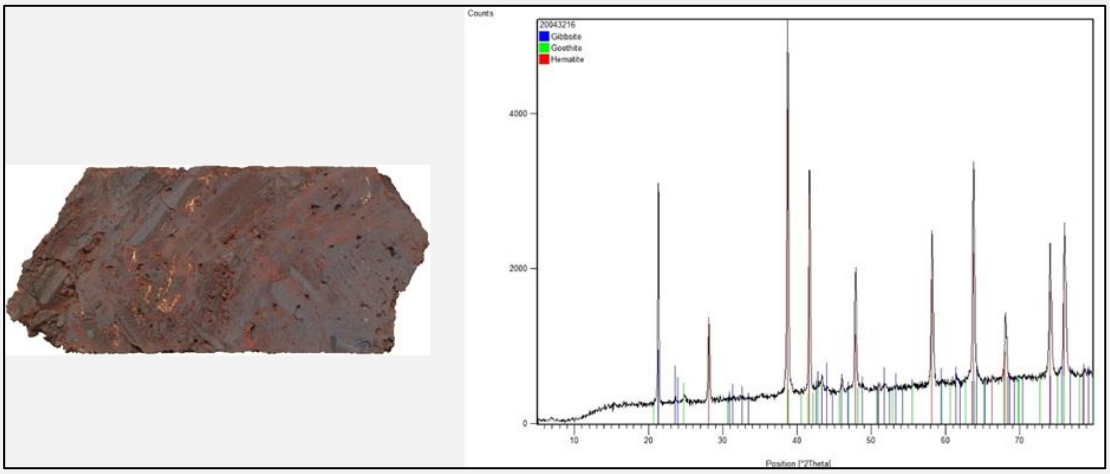

Figure 18. An X-ray diffractogram illustrating the dominant crystalline minerals identified in Sample SMZ 216.

Sample SMZ 217

XRD analysis confirms that this sample consists mainly of hematite and quartz (Figure 19).

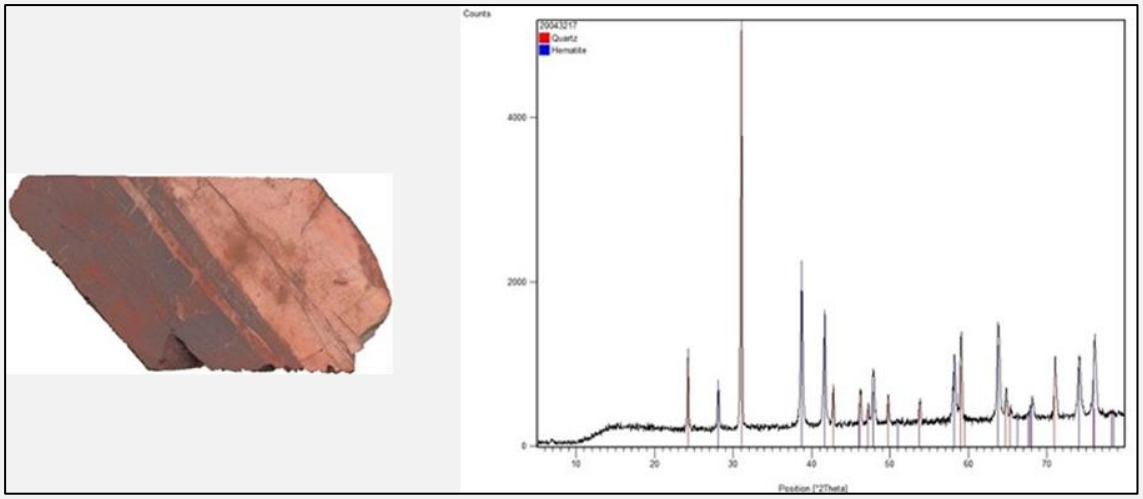

Figure 19. An X-ray diffractogram illustrating the dominant crystalline minerals identified in Sample SMZ 217.

Sample SMZ 218

XRD analysis confirms that this sample consists mainly of hematite and gibbsite (Figure 20).

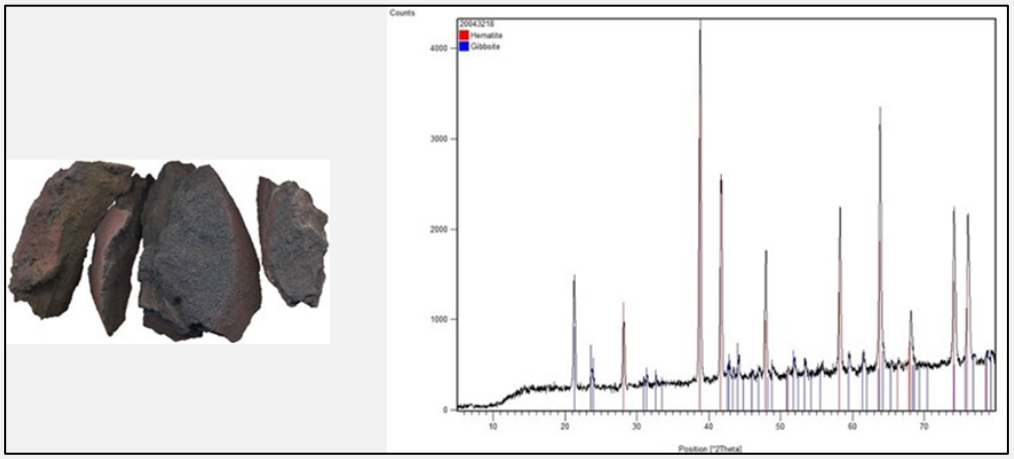

Figure 20. An X-ray diffractogram illustrating the dominant crystalline minerals identified in Sample SMZ 218.

Sample SMZ 219

XRD analysis confirms that this sample consists mainly of hematite (Figure 21).

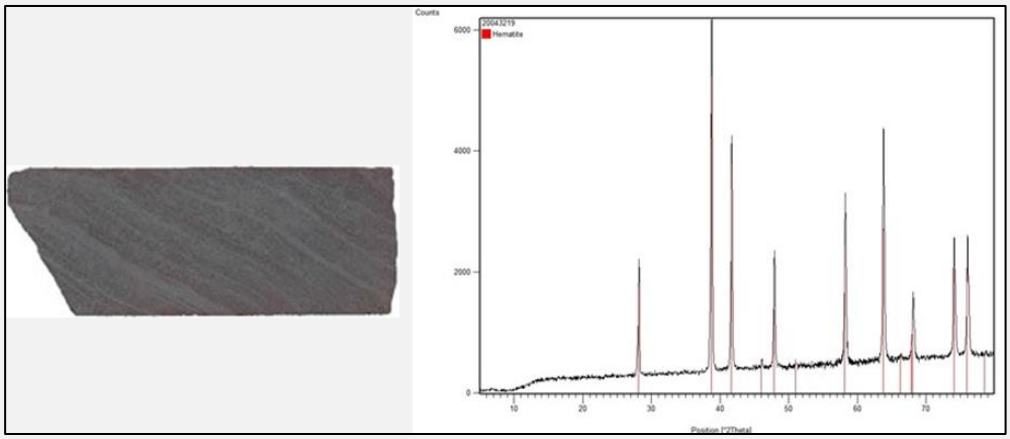

Figure 21. An X-ray diffractogram illustrating the dominant crystalline minerals identified in Sample SMZ 219.

Sample SMZ 220

XRD analysis confirms that this sample consists mainly of hematite, variscite ($AlPO_4 \cdot 2H_2O$), and anatase (TiO_2) (Figure 22).

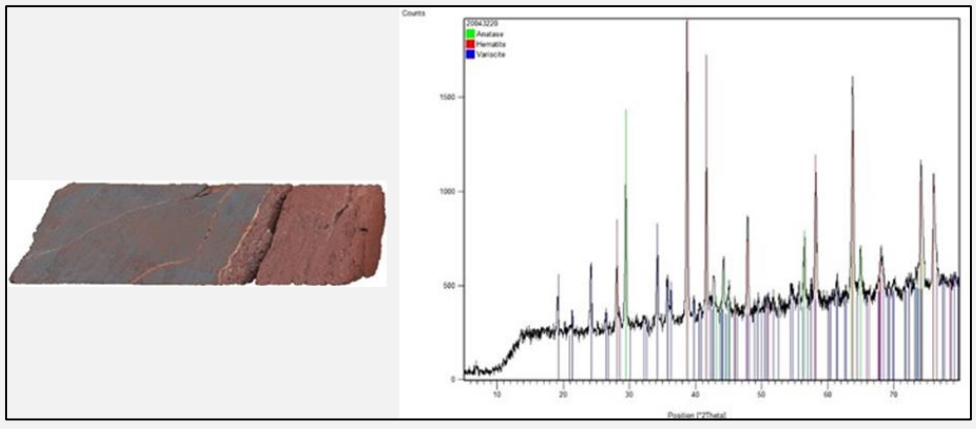

Figure 22. An X-ray diffractogram illustrating the dominant crystalline minerals identified in Sample SMZ 220.

Sample SMZ 222

XRD analysis confirms that this sample consists mainly of hematite (Figure 23).

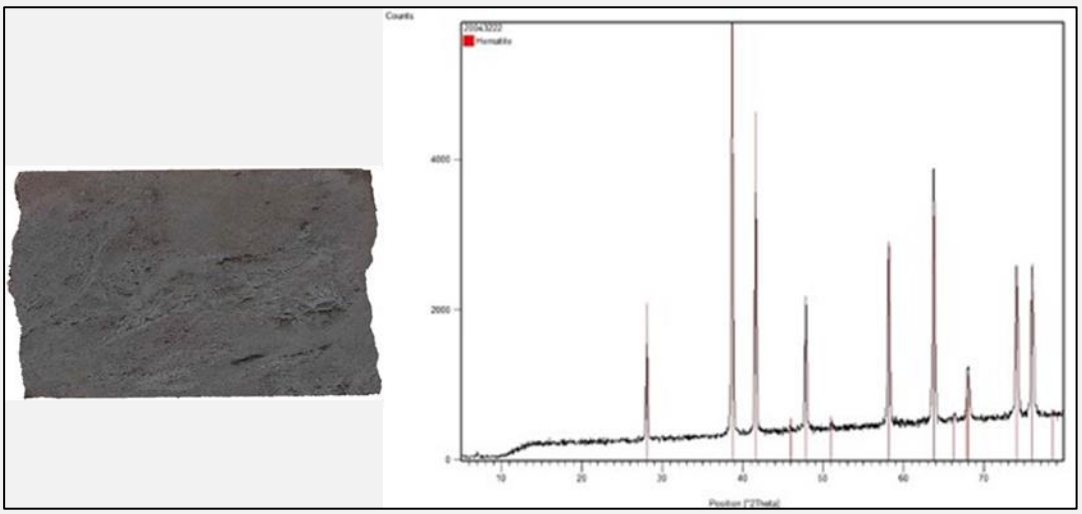

Figure 23. An X-ray diffractogram illustrating the dominant crystalline minerals identified in Sample SMZ 222.

Sample SMZ 227

XRD analysis confirms that this sample consists predominantly of hematite, gibbsite, and kaolinite group clays (Figure 24).

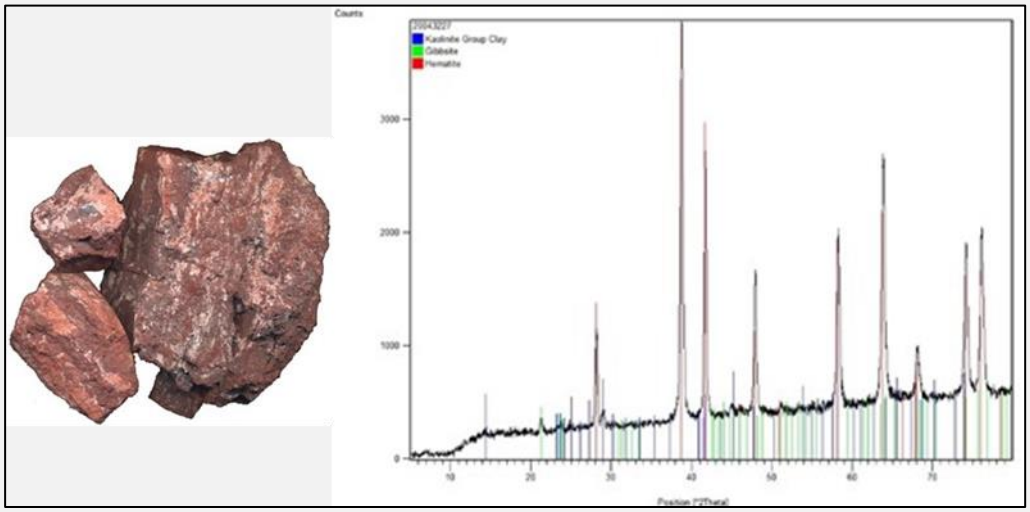

Figure 24. An X-ray diffractogram illustrating the dominant crystalline minerals identified in Sample SMZ 227.

DISCUSSION

The diffractometric analyses conducted on samples from the Zatua Hills BIFs clearly show that the primary iron ore mineral is hematite (Figures 18, 19, 20, 21, 22, and 23), with secondary phases primarily represented by gibbsite, variscite, kaolinite, goethite, and minor anatase (Figures 18, 20, 22, and 24). This hematite is produced through the oxidation of magnetite into pseudomorphic martite, as detailed in the microscopic observations.

The petrographic and diffractometric analyses of borehole samples from the Zatua Hills indicate that the BIFs have been enriched in iron ore. These analyses reveal significant silica leaching and subsequent enrichment in iron oxide, while deleterious elements or impurities such as aluminum (Al), phosphorus (P), and silicon (Si) are less prevalent in the samples (Figures 4a, 8, 10, 12, and 15). The processes of jointing, fracturing, folding, and shearing facilitated this leaching, leading to the removal of primary silica and the concentration of iron ores, particularly magnetite, martite, and hematite.

Quartz Content

The most common form of silica in the Zatua Hills BIFs is quartz, with variations ranging from chert to chalcedony. Chalcedony exhibits localized recrystallization, resulting in an increase in crystallite size. Recrystallized chalcedony/quartz veinlets cut through the more massive, fine-grained chalcedony and replace hematite-rich laminations along discordant fractures and concordant separations in the hematitic BIFs (Figure 4b). Quartz/chert appears to represent a later stage of mineralization than the hematitic BIF, possibly forming from the dissolution and subsequent re-precipitation of primary silicate gangue minerals (Harmsworth et al., 1990). Chalcedony also contains subordinate but significant amounts of secondary minerals, such as kaolinite and florencite [CeAl-phosphate: (Ce, La)$Al_3(PO_4)_2(OH)_6$] (Figures 3b & 4a).

Magnetite-Martite-Hematite Content

Magnetite ($Fe^{2+}Fe^{3+}{}_2O_4$) is the initial iron oxide identified in the BIF samples from the Zatua Hills, which has undergone extensive oxidation to martite (Fe_2O_3). The oxidation process begins around the magnetite grains, progressing along fractures and parallel to various crystallographic directions of magnetite. This oxidation leads to the development of martite aggregates, which form lattice networks that reflect the crystallographic planes of magnetite in relation to the oxygen cation planes observed in the cubic networks of magnetite and rhombohedral networks of hematite (Makuku et al., 2023).

These aggregates typically show irregular crystal outlines, indicating a lack of crystallographic equilibrium. The low degrees of recrystallization observed in most samples suggest a slight increase in temperature at some point after the oxidation process. However, these temperatures were neither high enough nor sustained long enough to allow the martite recrystallization process to continue fully (Makuku et al., 2023).

Martite-Microplaty Hematite Content

The circulation of supergene or hypogene fluids along zones of weakness facilitated the leaching of silica and the concentration of iron oxide, which created pores within the rock, allowing secondary minerals, including microplaty hematite, to precipitate. Microplaty hematite is an important constituent of high-grade iron ores, but it is virtually absent in iron-poor ores. It likely develops due to a slight increase in temperature, which also initiates the early recrystallization of martite.

These acicular hematite crystals are favorably oriented in the direction of leaching from the cavities, allowing elongated or scale-like crystals of microplaty hematite, also known as specularites, to develop on their outer surfaces (Figures 4, 6, 8, 10, and 13). The development of these crystals also contributes to the cementation of pores in the martite-rich fraction. The formation of microplaty hematite crystals reflects the introduction of additional iron into the system, leading to varying degrees of iron enrichment.

Microplaty hematite results from a thorough leaching process of BIFs, which can be both supergene, marked by the oxidation of magnetite by meteoric fluids and the recrystallization of pre-existing martite, and hypogene, marked by hematite precipitation from hydrothermal fluids and goethite dehydration (Powell et al., 1999; Morris, 1985).

According to the classic supergene-metamorphic model of Morris (1980, 1985), microplaty hematite replaces goethite, which requires temperatures in excess of 80°C (Langmuir, 1971). Morris's (1980, 1985) model suggests that martite-microplaty hematite ore genesis involves a two-step process: weathering of BIF followed by burial and low-grade metamorphism. During weathering, magnetite is transformed into martite and goethite, while subsequent metamorphism causes goethite to dehydrate into microplaty hematite.

Martite-microplaty hematite ore bodies exhibit textural preservation of the protore and a typical total porosity of approximately 30% (Dalstra et al., 2002).

Secondary Minerals Content

Secondary minerals likely originated from precipitation in pores, fractures, and other permeable zones under low-temperature, near-surface conditions. These minerals largely consist of goethite, secondary hematite, kaolinite, gibbsite, and variscite.

Thoroughly leached BIFs become porous and permeable, allowing for free fluid circulation in aquifers and providing suitable sites for the precipitation of secondary minerals (Makuku et al., 2023). These minerals often exhibit botryoidal or concretionary textures, indicative of precipitation along pores and the formation of a hard crust (goethite). Notably, secondary minerals such as gibbsite and variscite contribute to a significant portion of the deleterious elements or impurities in most samples.

All the mineral substitutions in the BIFs occurred through a succession of genetic processes, some of which were counteracted by subsequent events. The supergene process is the most recent and is responsible for transforming or leaching the rock, leading to iron enrichment (Morris, 1980, 1985, 2002; Harmsworth et al., 1990).

This observation supports a modified supergene-hypogene process associated with metamorphism (Beukes et al., 2003; Gutzmer et al., 2006; Lascelles, 2002, 2007), in which hydrothermal solutions, water from the dehydration of rocks hydrated by retrograde metamorphism, and meteoric water played major roles in the leaching of silica and the enrichment of itabirites in exploitable rich iron ores.

Martite-Goethite Content

Martite is the predominant iron-bearing mineral, accompanied by goethite, which occurs in voids and cavities (Figure 4). The precipitation of goethite in these voids resulted from the leaching of pre-existing minerals. The martite-goethite content is the result of desilicification through the action of hydrothermal fluids, similar to processes observed in the Jilling Langalata and Goa deposits in India (Roy & Venkatesh, 2009), the Hamersley Province deposits in Western Australia (Harmsworth et al., 1990), and Cerro Bolívar in Venezuela (Goldring, 2003).

Goethite occurs as a partial replacement of martite and forms botryoidal/concretionary aggregates within larger cavities and pore spaces between martite aggregates (Figure 4). Botryoidal textures are typical of open-space deposition. Qualitative SEM analysis of the goethite confirms that it contains minor amounts of Al, P, and Ti. Gibbsite and goethite represent relatively late stages of mineralization, likely precipitated from oxidizing fluids under near-surface weathering conditions.

Gibbsite Content

Gibbsite is the most common secondary mineral, found alone or in association with goethite and/or kaolinite in the pores of the rock. SEM observations show that gibbsite, composed primarily of Al, has variable water content and crystallinity. Gibbsite is a very late phase of precipitation, often linked to the core of goethite in the pores or to the center of transgressive goethite in fractures. Gibbsite likely formed due to near-surface alteration and subsequent precipitation from Al-rich fluids at low temperatures. Qualitative SEM analysis indicates that gibbsite typically contains minor but variable amounts of Fe (Figure 6b) and often exhibits varying degrees of ferruginization, likely representing partial replacement and/or fine intergrowths with goethite. Minor amounts of Si were also detected in gibbsite.

Anatase Content

Analysis of the samples taken from the boreholes clearly shows that the presence of Ti in the itabirites is associated with both phyllites and itabirites. Phyllites (chlorite, sericite schists) are considered low-temperature metamorphic rocks derived from argillites in this sedimentary basin. The affinity of titanium to this type of rock suggests that the form of titanium oxide associated with it is anatase, which corresponds to low-temperature, low-pressure metamorphism (Figure 11).

Anatase is a low-temperature form of TiO_2 and likely formed under the same conditions as variscite. Ti-bearing fluids generated during the oxidation and alteration of Ti-bearing oxides and silicates can precipitate anatase when Eh and pH conditions change lower in the alteration profile.

Variscite Content

In most cases, the presence of variscite is responsible for the high phosphorus content in the samples, often linked to strengite-variscite solid solutions [ideally formulated as $FePO_4 \cdot 2H_2O$ - $AlPO_4 \cdot 2H_2O$]. The composition of these minerals varies, with Al-rich solid solutions associated with gibbsite, while Fe-rich elements (strengite) are commonly present in areas devoid of Al-rich minerals. These minerals can contain high levels of P_2O_5, which have significant implications for the metallurgical quality of the iron ore.

Variscite and anatase likely formed due to the precipitation of supergene fluids at low temperatures under near-surface alteration conditions. Variscite generally forms from the reaction of P-bearing groundwater with Al-rich rocks in near-surface alteration environments (Figure 11b).

CONCLUSION

The petrographic and diffractometric analyses conducted on borehole samples from the Zatua Hills reveal that the BIFs are primarily hematitic, with magnetite (Fe_3O_4) being the most abundant iron oxide initially present. However, this magnetite underwent oxidation to martite, displaying a trellis texture before progressing to the hematite stage during certain phases of deposition. The formation of

iron ores was associated with a tectonic phase, during which various aluminum (Al), aluminum-phosphorus (Al-P), and aluminum-iron-phosphorus (Al-Fe-P) phases precipitated as late-stage vein fillings. These secondary minerals, primarily gibbsite and variscite-strengite solid solution series ($AlPO_4 \cdot 2H_2O$ and $FePO_4 \cdot 2H_2O$), along with kaolinite (rich in silica) and anatase (titanium oxide), were precipitated within the interstitial cavities leached between martite and hematite aggregates, forming botryoidal textures.

The transition from magnetite to martite is believed to have occurred at low temperatures, likely due to weak metamorphism. This is evidenced by the irregular contours of martite crystals observed microscopically, indicating that recrystallization had not yet reached equilibrium conditions. The presence of accessory minerals such as variscite and anatase at depth further supports the hypothesis that these minerals formed through the precipitation of low-temperature supergene fluids during rock alteration. Variscite, in particular, likely formed from the reaction of phosphorus-rich groundwater with aluminum-rich (peraluminous) rocks under alteration conditions.

The BIFs of the Zatua Hills exhibit rich iron ore with low levels of deleterious secondary minerals, suggesting potential industrial applications, provided that geochemical analyses are conducted to determine the precise percentages of iron oxides and associated minerals identified through petrographic and diffractometric analyses.

To enhance our understanding of the processes contributing to the enrichment of BIFs into iron ores, and to better characterize the depositional environment, further studies are essential. These should include isotopic and rare earth element geochemical analyses, as well as structural and metallogenic studies of the iron ores from the Zatua Hills and surrounding areas. Such studies will improve stratigraphic understanding, provide greater insight into the structural context, determine the source, temperature, and salinity of the fluids involved, and clarify whether the enrichment resulted from a single event or multiple episodes.

ACKNOWLEDGMENT

I would like to thank the team at Rio Tinto DRC for facilitating my fieldwork and data interpretation during my time in the Oriental project. I would also like to thank Professor Albert Ongendangenda of the University of Kinshasa for his contribution to the writing of this article.

REFERENCES

Allibone, A., Vargas, C., Mwandale, E., Kwibisa J., Jongens, R., Quick, S., Komarnisky, N., Fanning, M., Bird, F., MacKenzie, D., Turnbull, R., & Holliday, J. (2020). Orogenic Gold Deposits of the Kibali District, Neoarchean Moto Belt, Northeastern Democratic Republic of Congo. In *R. H. Sillitoe, R. J. Goldfarb, F. Robert, & S. F. Simmons, Geology of the World's Major Gold Deposits and Provinces*. Society of Economic Geologists. Society of Economic Geologists, Inc. SEG Special Publications, no. 23, pp. 185–201. https://doi.org/10.5382/SP.23.09

Beukes, N. J., Gutzmer, J., & Mukhopadhyay, J. (2003). The geology and genesis of high-grade hematite iron ore deposits. *Applied Earth Science, 112*(1), 18-25. https://doi.org/10.1179/037174503225011243

Bird, P. J. (2016). *Evolution of the Kibali Granite-Greenstone Belt, North East Democratic Republic of the Congo, and controls on gold mineralisation at the Kibali Gold Deposit* (Doctoral dissertation, Kingston University).

Borg, G., Shackleton, R. M. (1997). The Tanzania and NE-Zaire Cratons. In *de Wit, M. J., Ashwal, L. D. (Eds.), Greenstone Belts*. Oxford University Press, Oxford, pp. 608–619.

BRGM (Bureau de Recherches Géologiques et Minières). (1982). *A Geology and Mineral Map of Northeastern DRC Complied from by the BRGM (1980-1982) from a Field Survey in 1976 from Geological Maps Haut Zaire (Uele Area), Haut Zaïre (Ituri Area) at 1:500,000 Scale*.

Cahen, L., Snelling, N. J. (1966). *The geochronology of Equatorial Africa*. North-Holland Publishing Company, Amsterdam.

Cahen, L., Snelling, N. J., Delhal, J., Vail, J. R. (1984). *The Geochronology and Evolution of Africa*. Oxford Science Publishing, Clarendon Press, Oxford, UK.

Chamberlain, C. M. (2003). *Geology and genesis of the Bulyanhulu gold deposit, Sukumaland greenstone belt, Tanzania* (Doctoral dissertation, Imperial College London (University of London)).

Champion, D. C., & Sheraton, J. W. (1997). Geochemistry and Nd isotope systematics of Archaean granites of the Eastern Goldfields, Yilgarn Craton, Australia: implications for crustal growth processes. *Precambrian Research, 83*(1-3), 109-132. https://doi.org/10.1016/S0301-9268(97)00007-7

Clout, J. M. F., and Simonson, B. M., 2005, Precambrian Iron Formations and Iron Formation-Hosted Iron Ore Deposition. In *Jeffrey W. Hedenquist J. W., Thompson, J. F. H., Richard J. Goldfarb, R. J., & Richards, J. P. Economic Geology, v. 100th Anniversary* (pp. 643-679). https://doi.org/10.5382/AV100.20

Czarnota, K., Champion, D. C., Goscombe, B., Blewett, R. S., Cassidy, K. F., Henson, P. A., & Groenewald, P. B. (2010). Geodynamics of the eastern Yilgarn Craton. *Precambrian Research, 183*(2), 175-202. https://doi.org/10.1016/j.precamres.2010.08.004

Dalstra, H., Harding, T., Riggs, T., & Taylor, D. (2003). Banded iron formation hosted high-grade hematite deposits, a coherent group?. *Applied Earth Science, 112*(1), 68-72. https://doi.org/10.1179/037174503225011199

Davis, B. L., Rapp, G., & Walawender, M. J. (1968). Fabric and structural characteristics of the martitization process. *American Journal of Science, 266*(6), 482-496. https://doi.org/10.2475/ajs.266.6.482

de Wit, M. J., Guillocheau, F., & De Wit, M. C. (Eds.). (2015). *Geology and resource potential of the Congo Basin*. Springer Science & Business Media.

Goldring, D. C. (2003), Iron ore categorisation for the iron and steel industry. *Applied Earth Science, 112*(1), 5-17. https://doi.org/10.1179/0371745032501162

Gruner, J. W. (1926). Magnetite-martite-hematite. *Economic Geology, 21*(4), 375-393. https://doi.org/10.2113/gsecongeo.21.4.375

Gutzmer, J., Mukhopadhyay, J., Beukes, N. J., Pack, A., Hayashi, K., & Sharp, Z. D. (2006). Oxygen isotope composition of hematite and genesis of high-grade BIF-hosted iron ores. In *Memoir 198: Evolution of Early Earth's Atmosphere, Hydrosphere, and Biosphere - Constraints from Ore Deposits* (pp.257-268).

Harmsworth, R. A., Kneeshaw, M., Morris, R. C., Robinson, C. J., & Shrivastava, P. K. (1990). BIF-derived iron ores of the Hamersley Province. *Geology of the mineral deposits of Australia and Papua New Guinea, 1*, 617-642.

Kabete, J. M., Groves, D. I., McNaughton, N. J., & Mruma, A. H. (2012a). A new tectonic and temporal framework for the Tanzanian Shield: implications for gold metallogeny and undiscovered endowment. *Ore Geology Reviews, 48*, 88-124. https://doi.org/10.1016/j.oregeorev.2012.02.009

Kabete, J. M., McNaughton, N. J., Groves, D. I., & Mruma, A. H. (2012b). Reconnaissance SHRIMP U–Pb zircon geochronology of the Tanzania Craton: evidence for Neoarchean granitoid–greenstone belts in the Central Tanzania Region and the Southern East African Orogen. *Precambrian Research, 216*, 232-266. https://doi.org/10.1016/j.precamres.2012.06.020

Langmuir, D. (1971). Particle size effect on the reaction goethite= hematite+ water. *American Journal of Science, 271*(2), 147-156. https://doi.org/10.2475/ajs.271.2.147

Lascelles, D. F. (2002). A new look at old rocks—an alternative model for the origin of in situ iron ore deposits derived from banded iron formation. In *Proceedings of the Iron Ore 2002 conference, Perth* (pp. 107-126).

Lascelles, D. F. (2007). Black smokers and density currents: a uniformitarian model for the genesis of banded iron-formations. Ore Geology Reviews, 32(1-2), 381-411. https://doi.org/10.1016/j.oregeorev.2006.11.005

Lavreau, J. (1973). New data about the kilo-moto gold deposits (Zaïre) I. The district of Mongbwalu. *Mineralium Deposita, 8*, 1-6. https://doi.org/10.1007/BF00203345

Lavreau, J. (1980). Etude géologique du Zaïre septentrional. Génèse et évolution d'un segment lithosphérique archéen. *Unpublished Ph. D. Thesis, Université Libre de Bruxelles*.

Lavreau, J. (1982). The Archean and lower Proterozoic of Central Africa. *Revista brasileira de geociências, 12*(1-3), 187-192.

Lavreau, J. (1984). Vein and stratabound gold deposits of northern Zaire. Mineralium Deposita, 19, 158-165. https://doi.org/10.1007/BF00204680

Lavreau, J., & Ledent, D. (1975). Établissement du cadre géochronologique du Kibalien (Zaire). *Annales de la Société géologique de Belgique, 98*(1), 197-212.

Link, K., Koehn, D., Barth, M. G., Tiberindwa, J. V., Barifaijo, E., Aanyu, K., & Foley, S. F. (2010). Continuous cratonic crust between the Congo and Tanzania blocks in western Uganda. *International Journal of Earth Sciences, 99*, 1559-1573. https://doi.org/10.1007/s00531-010-0548-8

Makuku, L. M. (2018). Caractéristiques géologiques et pétrographiques des itabirites des Monts Zatua, Nord-Est de la RDC. *Revue de Congo Sciences, 6*, 141.

Makuku, L. M., Wetshondo, O. D., Kanda, N. V., Nzambe, K. K., & Ongendangenda, T. A. (2023). Geochemical Signature and Metalogeny of BIFs and Associated Iron Ore of Zatua Hills, Haut-Uele Province (DR Congo). *Journal of Geoscience and Environment Protection, 11*, 201-217. https://doi.org/10.4236/gep.2023.1110014

Manttari, I., Westerhof, P., Harma, P., Kigereigu, F., Koistinen, T., Kuosmanen, E., Lahaye, Y., Lehtonen, M.I., Makitie, H., Manninen, T., Pokki, J., & Virransalo, P. (2013). Mesoarchean to Neoproterozoic evolution of north Uganda: evidence from new U-Pb rock ages. *Abstract, 24rd CAG, Addis Ababa, 8th–14th January*.

Manya, S., Kobayashi, K., Maboko, M. A., & Nakamura, E. (2006). Ion microprobe zircon U–Pb dating of the late Archaean metavolcanics and associated granites of the Musoma-Mara Greenstone Belt, Northeast Tanzania: Implications for the geological evolution of the Tanzania Craton. *Journal of African Earth Sciences, 45*(3), 355-366. https://doi.org/10.1016/j.jafrearsci.2006.03.004

Morris, R. C. (1980). A textural and mineralogical study of the relationship of iron ore to banded iron-formation in the Hamersley Iron Province of Western Australia. *Economic Geology, 75*(2), 184-209. https://doi.org/10.2113/gsecongeo.75.2.184

Morris, R. C., & Wolff, K. H. (1985). Genesis of iron ore in banded iron-formation by supergene and supergene-metamorphic processes—a conceptual model. *Handbook of strata-bound and stratiform ore deposits, 13*, 73-235.

Morris, R. C. (2003). Iron ore genesis and post-ore metasomatism at Mount Tom Price. *Applied Earth Science, 112*(1), 56-67. https://doi.org/10.1179/037174503225011216

Morris, R. C., Tompkins, L. A., & Cowan, D. R. (2002). Discussion and Reply Opaque mineralogy and magnetic properties of selected banded iron-formations, Hamersley Basin, Western Australia. *Australian Journal of Earth Sciences, 49*(3), 579-586. https://doi.org/10.1046/j.0812-0099.2002.00935.x

Nyakecho, C., & Hagemann, S. G. (2014). An overview of gold systems in Uganda. *Australian Journal of Earth Sciences, 61*(1), 59-88. https://doi.org/10.1080/08120099.2013.831773

Poidevin, J. L. (1985). Le Protérozoïque supérieur de la République centrafricaine. *Annales-Musée royal de l'Afrique Centrale. Sciences géologiques,* (91).

Powell, C. M., Oliver, N. H., Li, Z. X., Martin, D. M., & Ronaszeki, J. (1999). Synorogenic hydrothermal origin for giant Hamersley iron oxide ore bodies. Geology, 27(2), 175-178. https://doi.org/10.1130/0091-7613(1999)027%3C0175:SHOFGH%3E2.3.CO;2

Roy, S., & Venkatesh, A. S. (2009). Mineralogy and geochemistry of banded iron formation and iron ores from eastern India with implications on their genesis. *Journal of Earth System Science, 118*, 619-641. https://doi.org/10.1007/s12040-009-0056-z

Sanislav, I. V., Wormald, R. J., Dirks, P. H. G. M., Blenkinsop, T. G., Salamba, L., & Joseph, D. (2014). Zircon U–Pb ages and Lu–Hf isotope systematics from late-tectonic granites, Geita Greenstone Belt: Implications for crustal growth of the Tanzania Craton. *Precambrian research, 242*, 187-204. https://doi.org/10.1016/j.precamres.2013.12.026

Sanislav, I. V., Kolling, S. L., Brayshaw, M., Cook, Y. A., Dirks, P. H., Blenkinsop, T. G., Mturi, M. I., & Ruhega, R. (2015). The geology of the giant Nyankanga gold deposit, Geita Greenstone Belt, Tanzania. *Ore Geology Reviews, 69*, 1-16. https://doi.org/10.1016/j.oregeorev.2015.02.002

Sanislav, I. V., Brayshaw, M., Kolling, S. L., Dirks, P. H., Cook, Y. A., & Blenkinsop, T. G. (2017). The structural history and mineralization controls of the world-class Geita Hill gold deposit, Geita Greenstone Belt, Tanzania. *Mineralium Deposita, 52*, 257-279. https://doi.org/10.1007/s00126-016-0660-1

Tompkins, L. A., & Cowan, D. R. (2001). Opaque mineralogy and magnetic properties of selected banded iron-formations, Hamersley Basin, Western Australia. *Australian Journal of Earth Sciences, 48*(3), 427-437. https://doi.org/10.1046/j.1440-0952.2001.00869.x

Turnbull, R., Allibone, A. H., Fanning, C. M., & Matheys, F. (2017). Geochronology, isotope chemistry, and relative prospectivity of Archean rocks in the northeast Democratic Republic of Congo, central Africa: St. Helier, Jersey, Channel Islands, Randgold Resources Ltd. *Unpublished report*.

Westerhof, A. B., Härmä, P., Isabirye, E., Katto, E., Koistinen, T., Kuosmanen, E., Lehto, T., Lehtonen, M. I., Makitie, H., Manninen, T., Manttari, I., Pekkala, Y., Pokki, J., Saalmann, K., & Virransalo, P. (2014). *Geology and geodynamic development of Uganda with explanation of the 1: 1,000,000 scale geological map*. Geological survey of Finland.

Woodtli, R. (1961). Iron ore resources of the North-Eastern Congo. *Economic Geology, 56*(8), 1385-1391. https://doi.org/10.2113/gsecongeo.56.8.1385